11-16-2017

Evolution of Galactic Outflows at $z \sim$ 0–2 Revealed with SDSS, DEEP2, and Keck Spectra

Yuma Sugahara
The University of Tokyo, Japan

Masami Ouchi
The University of Tokyo, Japan

Lihwai Lin
Academia Sinica, Taiwan

Crystal L. Martin
University of California - Santa Barbara

Yoshiaki Ono
The University of Tokyo, Japan

See next page for additional authors

Right click to open a feedback form in a new tab to let us know how this document benefits you.

Follow this and additional works at: https://uknowledge.uky.edu/physastron_facpub

Part of the Astrophysics and Astronomy Commons, and the Physics Commons

Repository Citation

Authors

Yuma Sugahara, Masami Ouchi, Lihwai Lin, Crystal L. Martin, Yoshiaki Ono, Yuichi Harikane, Takatoshi Shibuya, and Renbin Yan

Evolution of Galactic Outflows at *z* ~ 0–2 Revealed with SDSS, DEEP2, and Keck Spectra

Evolution of Galactic Outflows at $z \sim 0$–2 Revealed with SDSS, DEEP2, and Keck Spectra

Yuma Sugahara[1,2] , Masami Ouchi[1,3] , Lihwai Lin[4] , Crystal L. Martin[5] , Yoshiaki Ono[1], Yuichi Harikane[1,2] , Takatoshi Shibuya[1], and Renbin Yan[6]

[1] Institute for Cosmic Ray Research, The University of Tokyo, 5-1-5 Kashiwanoha, Kashiwa, Chiba 277-8582, Japan; sugayu@icrr.u-tokyo.ac.jp
[2] Department of Physics, Graduate School of Science, The University of Tokyo, 7-3-1 Hongo, Bunkyo, Tokyo, 113-0033, Japan
[3] Kavli Institute for the Physics and Mathematics of the Universe (WPI), The University of Tokyo, 5-1-5 Kashiwanoha, Kashiwa, Chiba 277-8583, Japan
[4] Institute of Astronomy & Astrophysics, Academia Sinica, Taipei 106, Taiwan, R.O.C.
[5] Department of Physics, University of California, Santa Barbara, CA 93106, USA
[6] Department of Physics and Astronomy, University of Kentucky, 505 Rose Street, Lexington, KY 40506-0055, USA
Received 2017 March 5; revised 2017 October 14; accepted 2017 October 19; published 2017 November 16

Abstract

We conduct a systematic study of galactic outflows in star-forming galaxies at $z \sim 0$–2 based on the absorption lines of optical spectra taken from SDSS DR7, DEEP2 DR4, and Keck (Erb et al.). We carefully make stacked spectra of homogeneous galaxy samples with similar stellar mass distributions at $z \sim 0$–2 and perform the multicomponent fitting of model absorption lines and stellar continua to the stacked spectra. We obtain the maximum (v_{max}) and central (v_{out}) outflow velocities and estimate the mass loading factors (η), a ratio of the mass outflow rate to the star formation rate (SFR). Investigating the redshift evolution of the outflow velocities measured with the absorption lines whose depths and ionization energies are similar (Na I D and Mg I at $z \sim 0$–1; Mg II and C II at $z \sim 1$–2), we identify, for the first time, that the average value of v_{max} (v_{out}) significantly increases by 0.05–0.3 dex from $z \sim 0$ to 2 at a given SFR. Moreover, we find that the value of η increases from $z \sim 0$ to 2 by $\eta \propto (1 + z)^{1.2 \pm 0.3}$ at a given halo circular velocity v_{cir}, albeit with a potential systematics caused by model parameter choices. The redshift evolution of v_{max} (v_{out}) and η is consistent with the galaxy-size evolution and the local velocity–SFR surface density relation and explained by high gas fractions in high-redshift massive galaxies, which is supported by recent radio observations. We obtain a scaling relation of $\eta \propto v_{cir}^{a}$ for $a = -0.2 \pm 1.1$ in our $z \sim 0$ galaxies that agrees with the momentum-driven outflow model ($a = -1$) within the uncertainties.

Key words: galaxies: formation – galaxies: evolution – galaxies: ISM – galaxies: kinematics and dynamics

1. Introduction

The large-scale structure of the universe is well explained by gravitational interactions based on the Lambda cold dark matter (ΛCDM) model (e.g., Springel et al. 2005). However, we need additional models to explain small-scale structures like galaxies, because these small scales are significantly affected by the baryon physics, such as gas cooling, radiation heating, star formation, and supernovae (SNe). In fact, there is a notable discrepancy between the shapes of the halo mass function predicted by numerical simulations of the ΛCDM model and the galaxy stellar mass function confirmed by observations (e.g., Somerville & Davé 2015). Theoretical studies suggest that this problem of the discrepancy is resolved by the feedback processes that regulate the star formation. Understanding the feedback processes is key to galaxy formation and evolution.

Galactic outflows driven by star-forming activities are one of the plausible sources of the feedback processes. The cold gas is accelerated by the starburst or the SNe and carried even to the outside of the halos. The lack of the cold gas thus quenches the star formation in the galaxies. Although the outflows make an impact on the star formation activity, their physical mechanisms are still poorly known. Theoretical studies propose some physical processes to launch the galactic outflows, such as the thermal pressure of the core-collapse SNe (e.g., Larson 1974; Chevalier & Clegg 1985; Springel & Hernquist 2003), the radiation pressure of the starburst (e.g., Murray et al. 2005; Oppenheimer & Davé 2006), and the cosmic-ray pressure (e.g., Ipavich 1975; Breitschwerdt et al. 1991; Wadepuhl & Springel 2011).

Since the outflow scale is very small in cosmological simulations, major numerical simulations carry out the outflows as subgrid physics (see Somerville & Davé 2015, for a recent review). On the other hand, some recent simulations employ the explicit thermal feedback generated by SNe with no outflows in subgrid physics and describe the relation between the outflow and galaxy properties (Barai et al. 2015; Muratov et al. 2015; Schaye et al. 2015). Muratov et al. (2015) and Barai et al. (2015) predict that outflow properties evolve toward high redshift based on their numerical models. Mitra et al. (2015) support the evolution of the outflow properties with their analytic model including empirical relations.

Optical and UV observations investigate the galactic outflows with emission lines (Heckman et al. 1990; Lehnert & Heckman 1996a, 1996b; Martin 1998) and absorption lines (Heckman et al. 2000; Schwartz & Martin 2004; Martin 2005; Rupke et al. 2005a, 2005b; Tremonti et al. 2007; Grimes et al. 2009; Martin & Bouché 2009; Alexandroff et al. 2015) that are found in the spectra of outflow galaxies ("down-the-barrel" technique). Particularly, the absorption lines are used to probe outflow velocities of star-forming galaxies at $z \sim 0$ (Chen et al. 2010; Chisholm et al. 2015, 2016), at $z \sim 1$ (Sato et al. 2009; Weiner et al. 2009; Kornei et al. 2012; Martin et al. 2012; Rubin et al. 2014; Du et al. 2016), and at $z > 2$ (Shapley et al. 2003; Steidel et al. 2010; Erb et al. 2012; Law et al. 2012; Jones et al. 2013; Shibuya et al. 2014). Moreover, absorption lines of background quasars are used to study the galactic outflows of foreground galaxies on the sight lines of the

background quasars (Bouché et al. 2012; Kacprzak et al. 2014; Muzahid et al. 2015; Schroetter et al. 2015, 2016).

Despite many observations in a wide redshift range, it is challenging to study the evolution of outflow velocities because of possible systematic errors included in different redshift samples. The literature uses various procedures to measure outflow velocities, such as nonparametric (Weiner et al. 2009; Heckman et al. 2015), one-component (Steidel et al. 2010; Kornei et al. 2012; Shibuya et al. 2014; Du et al. 2016), and two-component methods (Martin 2005; Chen et al. 2010; Martin et al. 2012; Rubin et al. 2014). Moreover, we should compare the samples of galaxies in the same stellar mass and star formation rate (SFR) ranges because the outflow properties depend on the stellar mass and SFR (i.e., Weiner et al. 2009; Erb et al. 2012; Heckman et al. 2015). Although Du et al. (2016) compare outflow velocities of star-forming galaxies at $z \sim 1$ with those at $z \sim 3$ that are derived with the same procedure, Du et al. (2016) cannot make similar galaxy samples at $z \sim 1$ and $z \sim 3$ owing to the lack of stellar mass measurements.

In this paper, we investigate the redshift evolution of galactic outflows found in the star-forming galaxies. We use spectra of galaxies at $z \sim 0$, 1, and 2 drawn from the Sloan Digital Sky Survey (SDSS; York et al. 2000), the Deep Evolutionary Exploratory Probe 2 (DEEP2) Galaxy Redshift Survey (Davis et al. 2003, 2007; Newman et al. 2013), and Erb et al. (2006a, 2006b), respectively. The combination of these data sets enables us to study the redshift evolution of outflow velocities based on the samples of star-forming galaxies with the same stellar mass and SFR ranges. Section 2 presents three samples of star-forming galaxies and our methods for spectrum stacking. We explain our analysis to estimate properties of outflowing gas in Section 3. We provide our results of the outflow velocities in Section 4 and discuss the redshift evolution of the outflow properties in Section 5. Section 6 summarizes our results. We calculate stellar masses and SFRs by assuming a Chabrier (2003) initial mass function (IMF). We adopt a ΛCDM cosmology with $\Omega_M = 0.27$, $\Omega_\Lambda = 0.73$, $h = H_0/(100 \text{ km s}^{-1} \text{ Mpc}^{-1}) = 0.70$, $n_s = 0.95$, and $\sigma_8 = 0.82$ throughout this paper, which are the same parameters as those used in Behroozi et al. (2013). All transitions are referred to by their wavelengths in vacuum. Magnitudes are in the AB system.

2. Data and Sample Selection

To study galactic outflows, we construct three samples at $z \sim 0$–2. A $z \sim 0$ sample is drawn from the SDSS Data Release 7 (DR7; Abazajian et al. 2009), a $z \sim 1$ sample is drawn from the DEEP2 Data Release 4 (DR4; Newman et al. 2013), and a $z \sim 2$ sample is drawn from Erb et al. (2006b). Each spectrum of galaxies in three samples does not have a signal-to-noise ratio (S/N) high enough for analysis of absorption lines. We therefore produce high-S/N composites by stacking the spectra. In this section, we describe each sample and explain the method of the spectrum stacking. Properties of the stacked spectra are listed in Table 1. We discuss the selection biases between three samples in Section 4.2.

2.1. Galaxies at $z \sim 0$

We select star-forming galaxies at $z \sim 0$ from the SDSS DR7 (Abazajian et al. 2009) main galaxy sample (Strauss et al. 2002). The spectra of these galaxies have a mean spectral resolution of $R \sim 2000$, a dispersion of 69 km s^{-1} pixel^{-1}, and a wavelength coverage spanning between 3800 and 9200 Å. These spectra are taken with fibers 3″ in diameter that are placed at the center of the galaxies. The SDSS imaging data are taken through a set of u, g, r, i, and z filters (Fukugita et al. 1996) using a drift-scanning mosaic CCD camera (Gunn et al. 1998).

Since our targets are active star-forming disk galaxies, we need some galaxy properties for sample selection. The galaxy properties are mainly taken from the MPA/JHU galaxy catalog.[7] Systemic redshifts z_{sys} are derived with observed spectra and a linear combination of the galaxy template spectra. Because this measurement may be affected by blueshifted absorption that outflowing gas produces, we compare z_{sys} in the MPA/JHU catalog with redshifts measured by fitting Hα emission lines alone with a Gaussian function. We find that the difference of the two redshifts is typically <5 km s^{-1} and negligible. Stellar masses M_* are obtained by the fitting to the photometry (Kauffmann et al. 2003; Salim et al. 2007). SFRs within the fiber (SFR$_{\text{fiber}}$) are measured from the extinction-corrected Hα emission-line flux, and total SFR is estimated by applying aperture correction with the photometry outside the fiber (Brinchmann et al. 2004). For our study, stellar masses and SFRs are converted from a Kroupa (2001) IMF to a Chabrier (2003) IMF with a correction factor of 0.93. SFR surface densities Σ_{SFR} are defined as SFR$_{\text{fiber}}/\pi R^2$, where R is the physical length corresponding to the SDSS 1″.5 aperture radius. The MPA/JHU catalog also includes the emission- and absorption-line fluxes (e.g., Hα, Hβ, [O III], [N II], and $D_n(4000)$; Tremonti et al. 2004) and the photometric properties (e.g., five photometric magnitudes). As a parameter to distinguish disk galaxies from ellipticals, we use the fracDeV (Abazajian et al. 2004), which is the coefficient of the best linear fitting that is a combination of exponential and de Vaucouleurs (1948) rules. When the fracDeVs of galaxies are less/greater than 0.8, they are defined as disk/elliptical galaxies. Because our targets are disk galaxies, we use the axial ratio of the exponential fitting. Using Table 8 in Padilla & Strauss (2008), we calculate the inclinations, i, of our galaxies from the r-band axial ratios and absolute magnitudes.

We use similar criteria to those used by Chen et al. (2010) to select the star-forming galaxies from the main galaxy sample (Strauss et al. 2002), which contains the galaxies with extinction-corrected Petrosian r magnitude in the range of $14.5 < r < 17.5$. The values of z_{sys} range from 0.05 to 0.18. To select active star-forming disk galaxies, we apply the criteria of $D_n(4000)$ less than 1.5 and r-band fracDeV less than 0.8. Active galactic nuclei (AGNs) are excluded with the classification by Kauffmann et al. (2003). We also exclude the galaxies whose SFRs or stellar masses are not derived in the MPA/JHU catalog. Moreover, we set two additional selection criteria for our study. First, we select the galaxies with $\Sigma_{\text{SFR}} \geqslant 10^{-0.8} M_\odot \text{ yr}^{-1} \text{ kpc}^{-2}$, which is above the empirical threshold $\Sigma_{\text{SFR}} > 0.1 M_\odot \text{ yr}^{-1} \text{ kpc}^{-2}$ for local galaxies to launch outflows (Heckman 2002). Second, we chose face-on

---

[7] The MPA/JHU galaxy catalog is available at http://www.mpa-garching.mpg.de/SDSS/DR7.

Table 1
Properties of the Stacked Spectra

| Sample	Line	Number	z	SFR $(M_\odot \ \mathrm{yr}^{-1})$	M_* $(M_\odot)$	v_{out} $(\mathrm{km \ s}^{-1})$	v_{max} $(\mathrm{km \ s}^{-1})$	η
(1)	(2)	(3)	(4)	(5)	(6)	(7)	(8)	(9)
z0-sample	Na I D	126	0.064	0.49	10.2	146 ± 5.2	221 ± 18	1.2 ± 0.84
	Na I D	113	0.075	0.69	10.3	152 ± 4.4	261 ± 12	1.2 ± 0.59
	Na I D	109	0.085	0.80	10.4	160 ± 4.5	299 ± 11	1.3 ± 0.53
	Na I D	138	0.11	0.93	10.5	144 ± 4.3	267 ± 11	0.83 ± 0.37
	Na I D	141	0.13	1.1	10.6	153 ± 4.3	327 ± 10	1.0 ± 0.37
	Na I D	123	0.14	1.3	10.8	165 ± 9.7	373 ± 20	1.1 ± 0.49
z1-sample	Mg I	662	1.4	1.0	9.99	220 ± 38	486 ± 64	4.6 ± 3.3
	Mg I	394	1.4	1.3	10.4	164 ± 16	309 ± 91	1.8 ± 3.2
	Mg I	277	1.4	1.5	10.6	175 ± 19	382 ± 98	1.2 ± 2.0
	Mg II	662	1.4	1.0	9.99	207 ± 5.0	445 ± 9	…
	Mg II	394	1.4	1.3	10.4	180 ± 16	442 ± 27	…
	Mg II	277	1.4	1.5	10.6	241 ± 7.1	569 ± 12	…
z2-sample	C II	25	2.2	1.4	10.3	428 ± 20	759 ± 20	3.6 ± 1.2
	C IV	25	2.2	1.4	10.3	445 ± 16	776 ± 16	…

Note. Column (3): number of galaxies used for a composite spectrum. Column (4): median redshift. Column (5): median global (i.e., aperture-corrected) star formation rate. Column (6): median stellar mass. Column (7): central outflow velocity defined in Section 4.1. Column (8): maximum outflow velocity defined in Section 4.1. Column (9): mass loading factor defined in Section 5.2.

galaxies whose inclinations are $i < 30°$ because the typical opening angle of the outflows is $<60°$ for the SDSS galaxies (Chen et al. 2010). There are 1321 galaxies that satisfy all of the selection criteria. The blue dashed line in Figure 1 indicates the normalized distribution of stellar masses for this sample. In order to make samples with similar stellar mass distribution at $z \sim 0$–2, we randomly select the high-mass galaxies from the sample to match the distribution of the sample at $z \sim 0$ to that of the sample at $z \sim 1$ (Section 2.2). The final galaxy sample contains 802 galaxies. We refer to the final sample as the $z0$-sample. The normalized distribution of stellar masses for the $z0$-sample is shown in Figure 1 with the blue solid line. The $z0$-sample is plotted in Figure 2 with the blue circles. The median stellar mass of the $z0$-sample is $\log(M_*/M_\odot) = 10.46$.

We produce high-S/N composites by stacking the spectra. Regarding each individual spectrum, the wavelength is shifted to the rest frame with z_{sys}, and the flux is normalized to the continuum around Na I D$\lambda\lambda$5891.58, 5897.56. Since bad pixels are identified as OR_MASK by the SDSS reduction pipeline, we exclude them in the same manner as done by Chen et al. (2010). These individual spectra are combined with an inverse-variance weighted mean. We divide the $z0$-sample into SFR bins where the composite spectra have S/N per pixel of 300 in the range of 6000–6050 Å.

2.2. Galaxies at $z \sim 1$

For our galaxies at $z \sim 1$, we use the DEEP2 DR4 (Newman et al. 2013).[8] The survey is conducted with DEIMOS (Faber et al. 2003) at the Keck II telescope. The DEEP2 survey targets galaxies with a magnitude limit of $18.5 < R_{\mathrm{AB}} < 24.1$ in four fields of the Northern Sky. In three of the four fields, the DEEP2 survey preselects these galaxies with B, R, and I photometry taken with the 12K camera at the Canada–France–Hawaii Telescope to remove galaxies at $z < 0.7$ (Coil et al. 2004). The spectra of these galaxies are taken with a 1200 line mm^{-1} grating and a 1″0 slit. The spectral setting gives
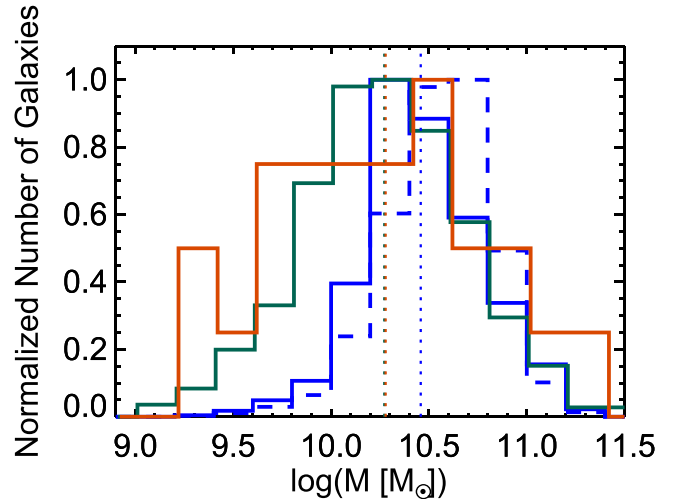
Figure 1. Normalized histograms of the stellar masses for the three samples. The blue, green, and orange solid lines indicate 802 galaxies in the $z0$-sample, 1337 galaxies in the $z1$-sample, and 25 galaxies in the $z2$-sample, respectively. The blue dashed line denotes the SDSS galaxies that satisfy the selection criteria. The blue, green, and orange vertical dotted lines show the median stellar masses of the $z0$-, $z1$-, and $z2$-samples, respectively. Each histogram is normalized to the maximum number of the bins.

$R \sim 5000$. The wavelength ranges from 6500 to 9100 Å. The public data are reduced with the DEEP2 DEIMOS Data pipeline (the *spec2d* pipeline; Cooper et al. 2012; Newman et al. 2013). In addition, we execute IDL routines for the flux calibration of the DEEP2 spectra (Newman et al. 2013). The IDL routines correct spectra for the overall throughput, chip-to-chip variations, and telluric contamination. After these corrections, the IDL routines calibrate fluxes of the spectra with the R- and I-band photometry. The flux calibration is accurate to 10% or better. Since the routines cannot calibrate some spectra correctly, we exclude the spectra from our sample.

We use galaxy properties taken from the DEEP2 DR4 redshift catalog. The catalog includes the absolute B-band

[8] The DEEP2 DR4 is available at http://deep.ps.uci.edu/DR4/home.html.
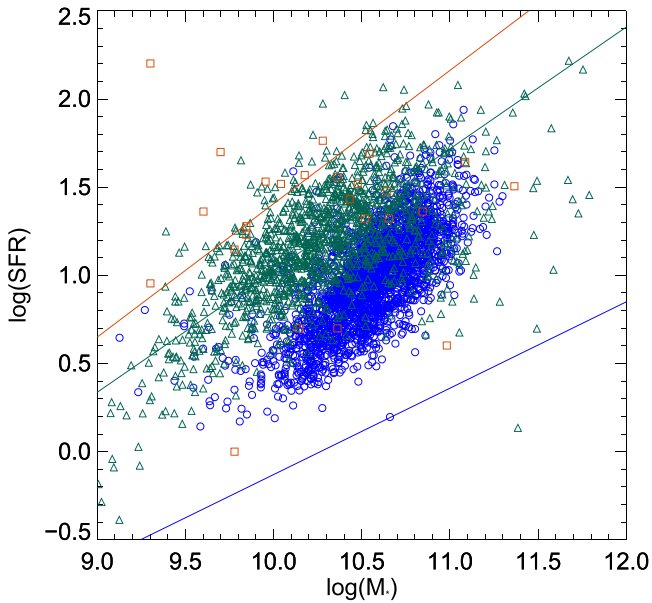
Figure 2. SFRs as a function of M_* for our three samples. The blue circles, green triangles, and orange squares indicate the galaxies of the z0-, z1-, and z2-samples, respectively. The intrinsic scatter of 0.2 dex (Mostek et al. 2012) is included in the data points to SFRs of the z1-sample for display purposes. The blue, green, and orange solid lines are the star-forming main sequences calculated with Equation (28) of Speagle et al. (2014) at $z \sim 0$, 1, and 2, respectively.

magnitude M_B, $(U - B)$ color in the rest frame, systemic redshift z_{sys}, and object classification. The last two parameters are determined by the *spec1d* redshift pipeline. The *spec1d* pipeline finds the best value of z_{sys} with galaxy-, QSO-, and star-template spectra to minimize χ^2 of the data and the templates (Newman et al. 2013). The error of z_{sys} is ~ 16 km s^{-1}. We also use $(B - V)$ color measured by C. N. A. Willmer (2017, private communication).

We use the Mg I $\lambda2852.96$ and Mg II $\lambda\lambda2796.35, 2803.53$ absorption lines in this study. These lines fall in the spectral range of DEEP2 spectra of galaxies at $1.2 < z < 1.5$. The Fe II $\lambda\lambda2586.65, 2600.17$ lines are also useful for outflow studies because they are free from resonance scattering. In the spectral range of the DEEP2 spectra, however, the Fe II lines are not available within the redshift range of the DEEP2 observation.

Since we need the spectra within which the Mg I and Mg II absorption lines fall, we first adopt the criteria used in Weiner et al. (2009). Weiner et al. (2009) select the spectra extending to 2788.7 Å in the rest frame. To avoid the AGN/QSO contamination, Weiner et al. (2009) exclude the galaxies at $z \geqslant 1.5$ or having the AGN classification of Newman et al. (2013). In addition to these criteria of Weiner et al. (2009), we remove galaxies that are at the red sequence (Willmer et al. 2006; Martin et al. 2012). We also remove the low-S/N galaxies that significantly affect the normalization procedure described below. Our final sample contains 1337 galaxies at $1.2 \lesssim z_{sys} < 1.5$ with the median value $\langle z \rangle = 1.37$. We refer to this sample as the z1-sample.

We estimate stellar masses and SFRs from equations in the literature. Stellar masses are calculated from M_B, $(U - B)$, and $(B - V)$ colors by Equation (1) of Lin et al. (2007). We rewrite the equation from Vega to AB magnitudes using the transformation in Willmer et al. (2006) and Blanton & Roweis (2007):

$$\begin{aligned}\log(M_*/M_\odot) = &-0.4(M_B - 5.48) + 1.737(B - V)\\ &+ 0.309(U - B) - 0.130(U - B)^2\\ &- 0.268z + 1.123.\end{aligned} \quad (1)$$

The normalized distribution of stellar masses for the z1-sample is shown in Figure 1 with the green line. The median stellar mass of the z1-sample is $\log(M_*/M_\odot) = 10.24$. SFRs are also calculated from M_B and $(U - B)$. Using Equation (1) and Table 3 of Mostek et al. (2012), we derive SFRs by

$$\begin{aligned}\log \text{SFR} = &\, 0.381 - 0.424(M_B + 21)\\ &- 2.925(U - B) - 2.603(U - B)^2.\end{aligned} \quad (2)$$

The quantities of the SFRs are calculated with a Salpeter (1955) IMF. To obtain the quantities in a Chabrier (2003) IMF, we apply a correction factor of 0.62. The z1-sample is plotted in Figure 2 with the green triangles.

Stacked spectra are produced in the same manner as in Section 2.1, but with three procedures for the z1-sample. The first procedure is to convert wavelength from air to vacuum by the method of Ciddor (1996). The second one is to normalize the flux at the continuum measured in the wavelength range around Mg II $\lambda\lambda2796.35, 2803.53$. The third one is to divide the z1-sample into three subsamples in low, medium, and high SFR bins.

2.3. Galaxies at $z \sim 2$

We use the sample of Erb et al. (2006b) for our sample at $z \sim 2$. The sample consists of BX/BM (Adelberger et al. 2004; Steidel et al. 2004) and MD (Steidel et al. 2003) galaxies, which are originally in the rest-frame UV-selected sample described by Steidel et al. (2004). The rest-frame UV spectra of galaxies are taken with the LRIS at the Keck I telescope, and the near-infrared (NIR) spectra are mainly taken with NIRSPEC (McLean et al. 1998) at the Keck II telescope. Since our aim is to analyze rest-frame UV absorption lines, we obtain the raw data taken with the 400/3400 grism of LRIS-B from 2002 to 2003 (PI Steidel) through the Keck Observatory Archive[9] (KOA). The spectral resolution is $R \sim 800$. The wavelength ranges from 3000 to 5500 Å.

The data are reduced with the XIDL LowRedux[10] pipeline. Right ascension (R.A.) and declination (decl.) of each galaxy are derived from the pixel values and the fits header of data with the program COORDINATES.[11] We find systematic errors of about $20''$ in results of COORDINATES. However, since some galaxies are observed with one mask at the same time, we can correct R.A. and decl. of them to be consistent with coordinates of Erb et al. (2006b). As shown in Steidel et al. (2010), this sample contains galaxy–galaxy pairs; the circumgalactic medium around foreground galaxies gives rise to absorption lines in the spectra of the background galaxies. For this reason, we remove six background galaxies of the galaxy–galaxy pairs from our sample. Finally, we obtain the spectra of 25 galaxies in the Erb et al. (2006b) sample. We refer to this sample as the z2-sample.

---

[9] KOA website: http://www2.keck.hawaii.edu/koa/public/koa.php.
[10] The XIDL LowRedux is available at http://www.ucolick.org/~xavier/LowRedux/.
[11] COORDINATES is available at http://www2.keck.hawaii.edu/inst/lris/coordinates.html.

We take z_{sys}, stellar masses, and SFRs of the $z2$-sample from Erb et al. (2006b). The systemic redshifts z_{sys} are determined by the Hα emission line on the NIR spectra. The typical rms error of z_{sys} is 60 km s^{-1} (Steidel et al. 2010). Stellar masses and SFRs are derived from the SED fitting with the U_n, G, R, J, and K-band magnitudes. The mid-infrared magnitudes taken with Infrared Array Camera on the *Spitzer Space Telescope* are also used, if they are available. The normalized distribution of stellar masses for the $z2$-sample is shown in Figure 1 with the orange line. The $z2$-sample is plotted in Figure 2 with the orange squares. The median stellar mass of the $z2$-sample is $\log(M_*/M_\odot) = 10.28$.

Stacked spectra are produced in the same manner as in Section 2.1, but with four procedures for the $z2$-sample: (1) to convert the wavelength from air to vacuum; (2) to normalize the flux in the wavelength range between 1410 and 1460 Å; (3) not to exclude bad pixels, since they are not detected by the pipeline; and (4) not to divide the $z2$-sample into subsamples.

3. Analysis

We analyze metal absorption resonance lines in the galaxy spectra to study the outflow properties. The absorption lines are Na I D $\lambda\lambda5891.58$, 5897.56 for the $z0$-sample; Mg I $\lambda2852.96$ and Mg II $\lambda\lambda2796.35$, 2803.53 for the $z1$-sample; and Si II $\lambda1260$, C II $\lambda1334.53$, Si II $\lambda1527$, and C IV $\lambda\lambda1548.20$, 1550.78 for the $z2$-sample. We assume that absorption profiles consist of three components: the intrinsic component composed of the stellar absorption and the nebular emission lines, the systemic component produced by the static gas in the interstellar medium (ISM) of the galaxies, and the outflow component produced by the outflowing gas from the galaxies. The stellar atmospheres of cool stars specifically give rise to the strong Na I D absorption, which impacts the results of the outflow analysis (Chen et al. 2010). The stellar atmospheres also provide moderate absorption features of Mg I, Mg II, Si II, C II, and C IV (Rubin et al. 2010; Coil et al. 2011; Steidel et al. 2016). Additionally, the static gas in the ISM produces absorption lines at the systemic velocity, while the outflowing gas makes blueshifted absorption lines (e.g., Martin 2005; Chen et al. 2010; Rubin et al. 2014). We follow the procedures of the analysis shown in Chen et al. (2010). Below, we explain the procedures that are made in two steps. First, we determine the stellar continuum of the stacked spectra for the intrinsic components of the absorption lines. Second, we model the absorption lines with the stellar continuum and obtain the outflow components.

3.1. Stellar Continuum Determination

We determine the stellar continuum with simple stellar population (SSP) models. For the $z0$-sample, we adopt Bruzual & Charlot (2003, BC03) SSP models, which have a high spectral resolution in the wavelength of the SDSS spectra. We use the 30 template spectra with 10 ages of 0.005, 0.025, 0.1, 0.29, 0.64, 0.90, 1.4, 2.5, 5, and 11 Gyr and three metallicities of $Z = 0.004$, 0.02, and 0.05. On the other hand, for the $z1$- and $z2$-samples, we adopt Maraston et al. (2009) SSP models based on a Salpeter IMF because the template spectra of BC03 models have a low spectral resolution at wavelengths less than 3300 Å. Maraston et al. (2009) models have a high spectral resolution of $R \sim 10000$ in the wavelength range of
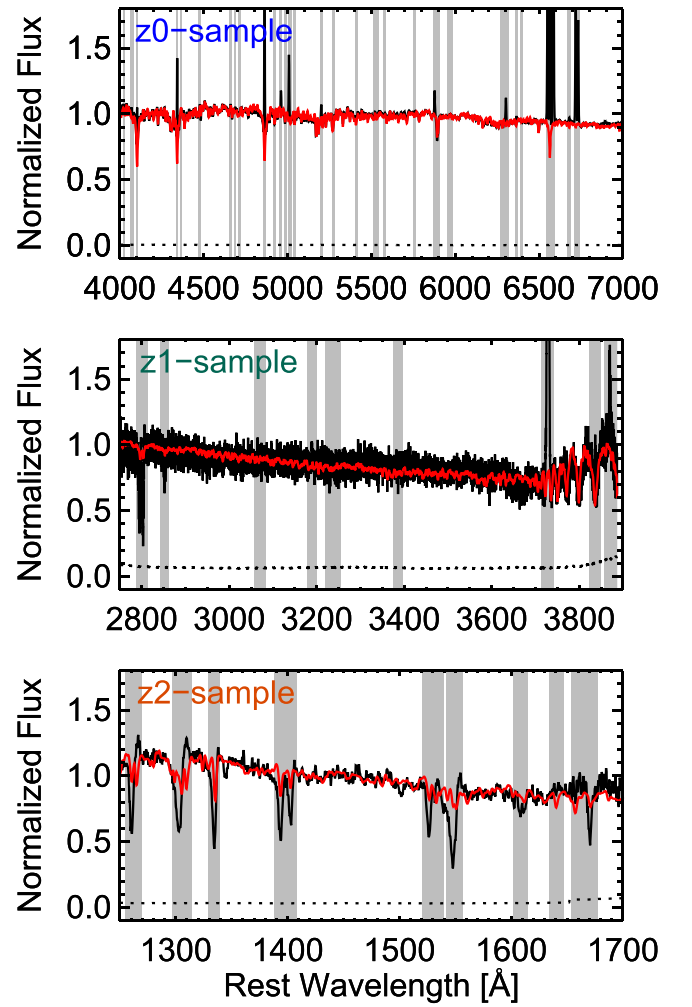
Figure 3. Examples of the stacked spectra (black line) and the best-fitting continuum models (red line). The spectra of the $z0$-, $z1$-, and $z2$-samples are shown from top to bottom. The wavelength range shown in this figure is used for the stellar continuum fitting, except for the gray shading. The dotted lines denote 1σ uncertainties of the spectra.

1000–4700 Å. We use the 30 template spectra with 10 ages of 1, 5, 25, 50, 100, 200, 300, 400, 650, and 900 Myr and three metallicities of $Z = 0.001$, 0.01, and 0.02. For all samples, each template spectrum is convolved with the stellar velocity dispersion of each stacked spectrum. We construct the best-fitting models of the stacked spectra with a linear combination of the template spectra applying the starburst extinction curve of Calzetti et al. (2000) by the IDL routine MPFIT (Markwardt 2009). We make the linear combination of all 30 template spectra and fit it to the $z0$-sample composite spectra, which have high S/N. We perform the same analysis of the $z1$- and $z2$-sample spectra, but we use the linear combination of 10 template spectra of a fixed metallicity. Since our main results are insensitive to differences of metallicities, we use $Z = 0.01$ for $z1$- and $z2$-samples. The rest-frame wavelength ranges used for fitting are 4000–7000 Å for the $z0$-sample, 2750–3500 Å for the $z1$-sample, and 1200–1600 Å for the $z2$-sample. In the fitting we omit the wavelength ranges of all of the emission and absorption lines except for those made by the stellar atmosphere. Figure 3 shows the stacked spectra (black) and the best-fitting models (red) of the $z0$-, $z1$-, and $z2$-samples.

3.2. Outflow Profile Estimate

With the best-fitting models of the stellar continuum, we estimate the systemic and outflow components of the absorption lines. The normalized line intensity $I_{obs}(\lambda)$ is assumed to be expressed by three components:

$$I_{obs}(\lambda) = I_{int}(\lambda)\, I_{sys}(\lambda)\, I_{out}(\lambda), \qquad (3)$$

where $I_{int}(\lambda)$ is the intrinsic component and $I_{sys}(\lambda)$ and $I_{out}(\lambda)$ are the systemic and the outflow components whose continua are normalized to unity, respectively. We use the stellar continuum given in Section 3.1 for $I_{int}(\lambda)$, except for Na I D that are explained later in case (ii). We adopt a model made from a set of following two equations for each of the systemic and outflow components (Rupke et al. 2005a). In this model, the normalized line intensity $I(\lambda)$ is given by

$$I(\lambda) = 1 - C_f + C_f e^{-\tau(\lambda)}, \qquad (4)$$

where $\tau(\lambda)$ is the optical depth and C_f is the covering factor. Although C_f may be a function of wavelength (Martin & Bouché 2009), we assume that C_f is independent of wavelength. Under the curve-of-growth assumption, the optical depth is written with a Gaussian function as

$$\tau(\lambda) = \tau_0 e^{-(\lambda - \lambda_0)^2 / (\lambda_0 b_D / c)^2}, \qquad (5)$$

where c is the speed of light, τ_0 is the optical depth at the central wavelength λ_0 of the line, and b_D is the Doppler parameter in units of speed. There are four parameters for each of $I_{out}(\lambda)$ (i.e., $\lambda_{0,out}$, $\tau_{0,out}$, $C_{f,out}$, and $b_{D,out}$) and $I_{sys}(\lambda)$ (i.e., $\lambda_{0,sys}$, $\tau_{0,sys}$, $C_{f,sys}$, and $b_{D,sys}$). Because the central wavelength $\lambda_{0,sys}$ of $I_{sys}(\lambda)$ is fixed to the rest-frame wavelength λ_{rest}, the model of $I_{obs}(\lambda)$ includes seven (=4 + 3) free parameters in total.

Equation (3) is modified in the following two cases: (i) The first case is applied for the doublet lines (Na I D, Mg II, and C IV). We define the optical depth of the blue and red lines of the doublet as $\tau_B(\lambda)$ and $\tau_R(\lambda)$, whose central wavelengths are $\lambda_{0,B}$ and $\lambda_{0,R}$, respectively. The total optical depth is written as $\tau(\lambda) = \tau_B(\lambda) + \tau_R(\lambda)$. Because the blue lines have oscillator strengths twice as high as the red lines for all of the doublet lines, the central optical depths of the blue lines $\tau_{0,B}$ are related to those of the red lines $\tau_{0,R}$ by $\tau_{0,R} = \tau_{0,B}/2$. The ratio of the central wavelengths $\lambda_{0,B}/\lambda_{0,R}$ of the outflow component is fixed to the rest-frame doublet wavelength ratio. We assume that b_D and C_f for the blue and red lines are the same since these lines should arise from the same gas clumps. The number of free parameters therefore remains unchanged. (ii) The second case is applied for Na I D, which has a neighboring emission line He I $\lambda5877.29$. We model the emission-line profile $I_{emi}(\lambda)$ of He I using a Gaussian function with two additional free parameters. In this case, the intrinsic component of Equation (3) is expressed as

$$I_{int}(\lambda) = I_{cont}(\lambda) + I_{emi}(\lambda), \qquad (6)$$

where $I_{cont}(\lambda)$ is the stellar continuum given in Section 3.1. For Na I D, there are a total of nine (=7 + 2) free parameters in $I_{obs}(\lambda)$, composed of seven free parameters of Equations (4)–(5) and the two parameters of the Gaussian function $I_{emi}(\lambda)$.

We carry out the model fitting and obtain the best-fit model of each absorption line with MPFIT. We place three constraints of the parameters for the fitting. First, since Martin & Bouché

(2009) show that covering factors of Na I D and Mg I are smaller than those of Mg II, we limit the range of $C_{f,out}$ to $0 \leqslant C_{f,out} \leqslant 0.2$ ($0 \leqslant C_{f,out} \leqslant 1$) for Na I D and Mg I (the other absorption lines). Second, we fix $b_{D,out}$ of the z2-sample at 130 km s^{-1}, which is the average value of the z1-sample, and we constrain $b_{D,sys}$ of the z2-sample at $\leqslant 150$ km s^{-1}. Third, we set the upper limit of $\tau_{0,out}$ so that the column densities of hydrogen $N(H)$ calculated with Equations (15) and (16) are as much as $\log N(H) \leqslant 21.5$ (Rupke et al. 2005a; Martin 2006; Rubin et al. 2014). Figure 4 shows the examples of the fitting results. Our procedure provides the reasonable results and detects the blueshifted outflow components that are shown with the dashed blue lines in Figure 4.

Figure 4 indicates that the best-fit Na I D profile is composed of the large intrinsic and small outflow components. Since the intrinsic component is estimated with the BC03 SSP model, a different SSP model may systematically affect our results. To evaluate the systematics, we analyze the Na I D lines with another SSP model, Maraston & Strömbäck (2011, MS11) based on MILES. The central and maximum outflow velocities estimated with MS11 are very similar to those estimated with BC03; their differences are only 10–30 km s^{-1}. The differences come from the fact that the Na ID stellar absorption line of MS11 is shallower than that of BC03. This result is consistent with the appendix in Chen et al. (2010), which evaluates the systematics that different SSP models give.[12]

We note that there exists a plausible shallow absorption around 1540 Å in the bottom right panel of Figure 4. This shallow absorption may arise from stellar winds of young stars that broaden the C IV absorption line (Schwartz & Martin 2004; Schwartz et al. 2006). Although the outflow components are determined by a deep C IV absorption line, the shallow absorption may produce a systematic uncertainty of the outflow velocities. Du et al. (2016) reproduce the shallow absorption with SSP models from Leitherer et al. (2010) that includes the predicted effects of the stellar wind. Because we do not use the C IV absorption line for discussion, the results of C IV are not relevant to our main scientific results.

4. Results

4.1. Outflow Velocity

We define the velocity of the outflowing gas in two ways: the central outflow velocity $v_{out} = c(\lambda_{rest} - \lambda_{0,out})/\lambda_{rest}$ and the maximum outflow velocity $v_{max} = c(\lambda_{rest} - \lambda_{max})/\lambda_{rest}$. The maximum wavelength λ_{max} is defined as

$$\lambda_{max} = \lambda_{0,out} - \lambda_{0,out} \frac{b_{D,out}}{c} \sqrt{-\ln\left(\frac{1}{\tau_{0,out}} \ln \frac{1}{0.9}\right)}, \qquad (7)$$

at which the blue side of the outflow component reaches 90% of the flux from $1 - C_f$ to unity, i.e., $I_{out}(\lambda_{max}) = 0.9(1 - C_f)$. The central outflow velocity v_{out} is the central velocity of the outflowing gas, which represents the bulk motion of the gas. In contrast, the maximum outflow velocity v_{max} reflects the gas motion at the largest radii of the outflows, based on the simple scenario that the outflowing gas is accelerated toward the

---

[12] As shown in Section 4.2, a decrease in outflow velocities at $z \sim 0$ strengthens the redshift evolution of outflow velocities from $z \sim 0$ to 2. Thus, systematics given by SSP models do not change our conclusion.
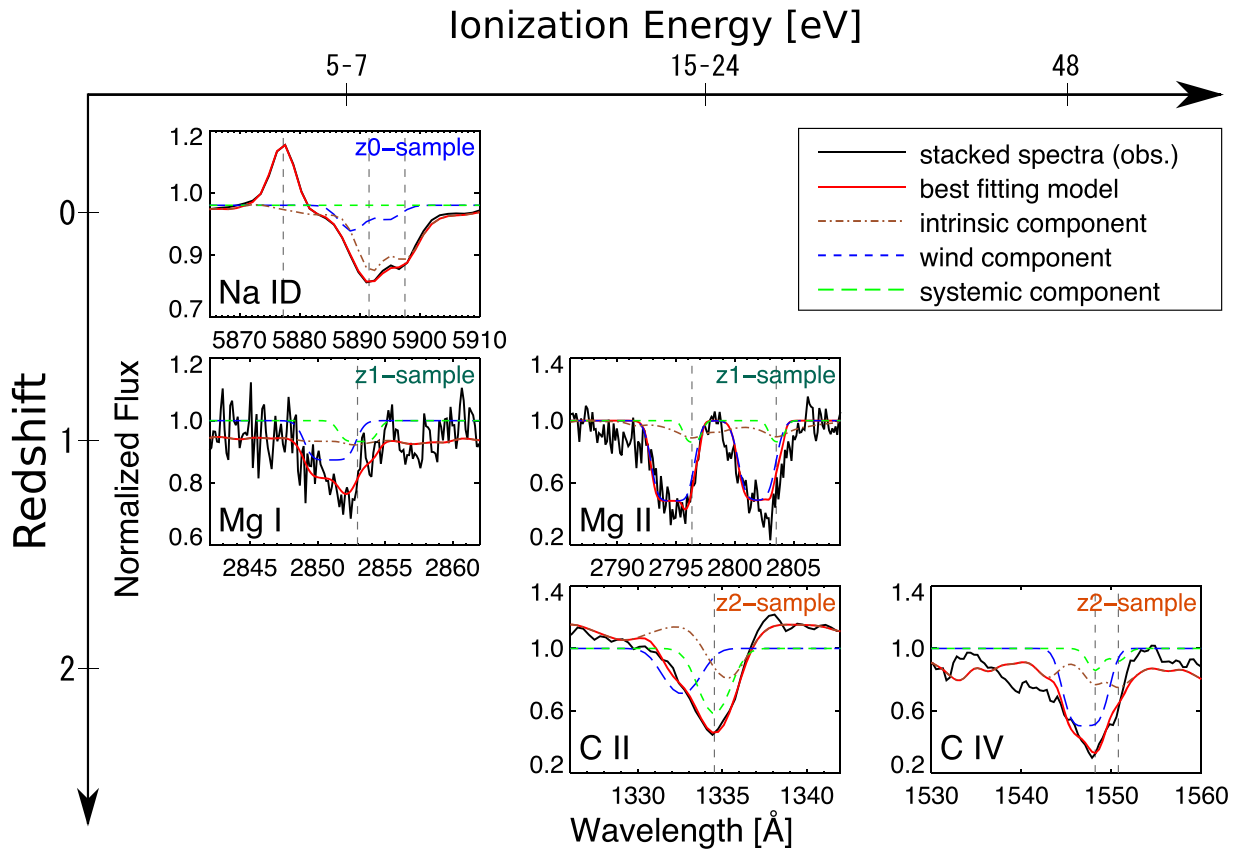
Figure 4. Examples of the stacked spectra around the absorption lines (black line). The red lines represent the best-fitting models. The dot-dashed brown, dashed blue, and long-dashed green lines indicate the breakdowns of the lines for the intrinsic, wind, and systemic components, respectively. In this figure, the redshift (the ionization energy) increases from top to bottom (from left to right). The ions of the absorption lines are written in the bottom left corner of the panels, and the samples are written in the top right corner. The vertical dashed gray lines denote the rest-frame wavelengths of the absorption lines, except for the line at 5877.29 Å in the top left panel, which represents the wavelengths of He I emission.

outside of the halo (Martin & Bouché 2009). Therefore, v_{max} is the indicator of whether the outflowing gas can escape the galactic halo to the intergalactic medium (IGM).

Figures 5–7 show v_{max} and v_{out} as a function of SFRs. In Figure 5, v_{max} and v_{out} of the z0-sample (shown with the blue circles) are as high as those of galaxies at $z \sim 0$ in the literature (shown with the open symbols). We perform a power-law fitting to v_{max} and v_{out} with the form of $V = V_1 \, SFR^{\alpha}$. The best-fit parameters are $V_1 = 174 \pm 9$ and $\alpha = 0.25 \pm 0.04$ for $V = v_{max}$ and $V_1 = 145 \pm 12$ and $\alpha = 0.03 \pm 0.03$ for $V = v_{out}$. The parameter α for v_{max} shows a significant correlation between v_{max} and SFR. Our measurement of $\alpha = 0.25 \pm 0.04$ for v_{max} is consistent with the results of Martin (2005) and Martin et al. (2012), who claim that v_{max} has a steep slope of $\alpha = 0.35 \pm 0.06$. On the other hand, the parameter α for v_{out} suggests no correlation with SFR, which is supported by previous studies (Chen et al. 2010; Martin et al. 2012).

Figure 6 compares v_{max} and v_{out} of the z1-sample with those of galaxies at $z \sim 1$ in the literature. The z1-sample shown with the green symbols is in good agreement with the literature. Particularly, the values of v_{max} are consistent with those in Weiner et al. (2009), who use the DEEP2 DR3 spectra. We also find a weak positive scaling relation between v_{out} and SFR. In the literature, whereas v_{out} of individual galaxies show no correlation (Kornei et al. 2012; Martin et al. 2012; Rubin et al. 2014), those of stacked galaxies show a positive

correlation (Weiner et al. 2009; Bordoloi et al. 2014). The positive scaling relations in Figure 6 (green symbols) are consistent with the previous results of the stacked galaxies.

Figure 7 shows the outflow velocities estimated with the C II, Si II, and C IV lines of the z2-sample. Unlike the C II and C IV lines, the Si II $\lambda\lambda$1260 and 1527 lines have their associated Si II* $\lambda\lambda$1265 and 1533 fluorescent emission lines, respectively. For this reason, emission filling of the Si II absorption lines may be weaker than that of the C II and C IV lines. Figure 7 illustrates that this difference of the lines does not change the outflow velocities in our analysis. In the remainder of this paper, we use the C II line to estimate outflow parameters of the z2-sample.
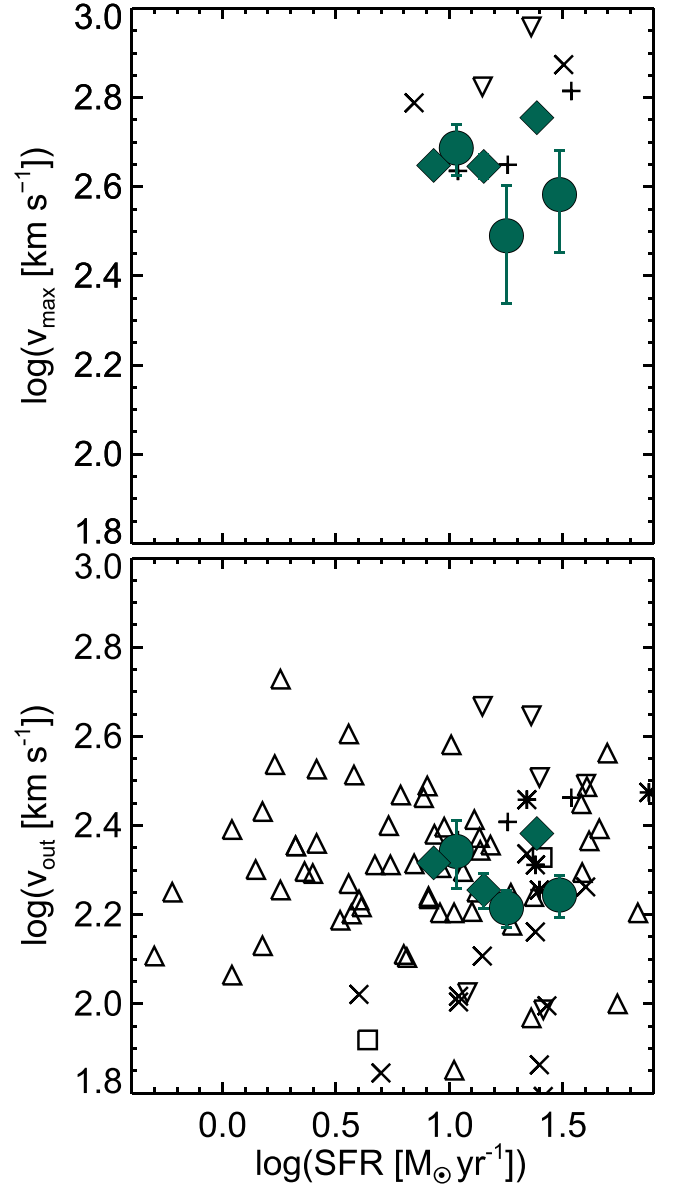
Steidel et al. (2010) study the outflow velocities (Δv_{IS}) of the UV-selected galaxies at $z \sim 2$ with the sample drawn from Erb et al. (2006b). The mean outflow velocity ($\langle\Delta v_{IS}\rangle = -164 \pm 16$ km s^{-1}) is lower than v_{out} of the z2-sample. This arises from different methods to measure the velocities: the outflow velocity become lower with the one-component fitting than with the two-component fitting. Therefore, it is reasonable that Δv_{IS} is lower than v_{out}, even though the z2-sample is a subsample drawn from Erb et al. (2006b). Steidel et al. (2010) also find that the scaling relation of central outflow velocities at $z \gtrsim 2$ is flatter than that at $z < 2$, but we cannot mention the scaling relation of the z2-sample as a result of the small sample size.
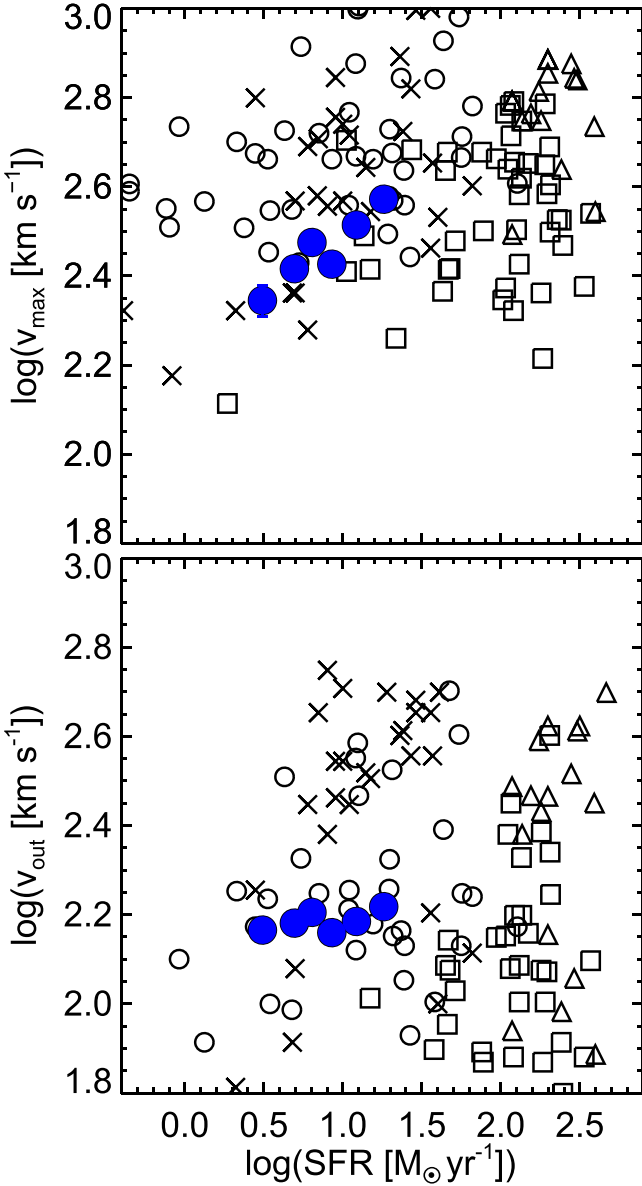
Figure 5. Outflow velocities at $z \sim 0$. Top: maximum outflow velocities (blue filled circle) of the $z0$-sample as a function of SFRs. Error bars denote the 1σ fitting error. The open symbols show the maximum outflow velocities of local galaxies in the literature: Heckman et al. (2015; cross), Martin (2005; triangle), Rupke et al. (2005b; square), and Chisholm et al. (2015; circle). Bottom: central outflow velocities of the $z0$-sample. The symbols are the same as those in the top panel of this figure.
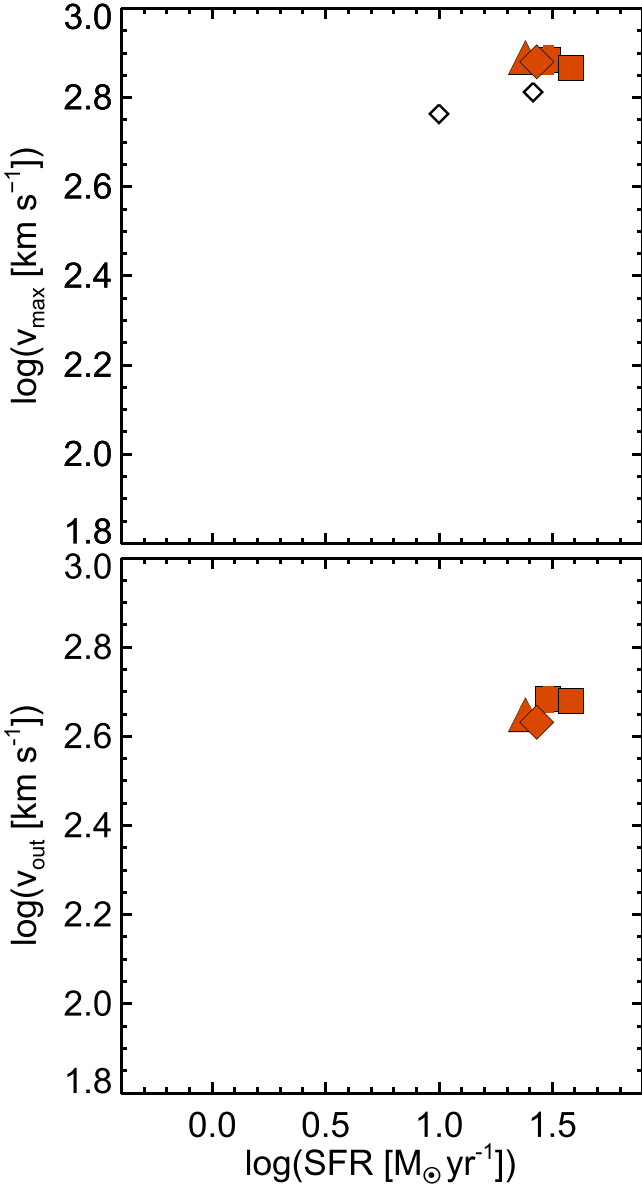
Figure 6. Same as Figure 6, but for the outflow velocities at $z \sim 1$. Top: maximum outflow velocities of the $z1$-sample for Mg I and Mg II (green filled circle and diamond, respectively) as a function of SFRs. Error bars denote the 1σ fitting errors. The open symbols show the maximum outflow velocities of galaxies at $z \sim 0.5$–1 in the literature: Kornei et al. (2012; cross), Rubin et al. (2014; triangle), Bordoloi et al. (2014; square), Weiner et al. (2009; plus sign), Martin et al. (2012; downward-pointing triangle), and Du et al. (2016, asterisk). Bottom: central outflow velocities of the $z1$-sample. The symbols are the same as those in the top panel. In both panels, the green diamonds are offset in SFR by 0.1 dex for clarity.
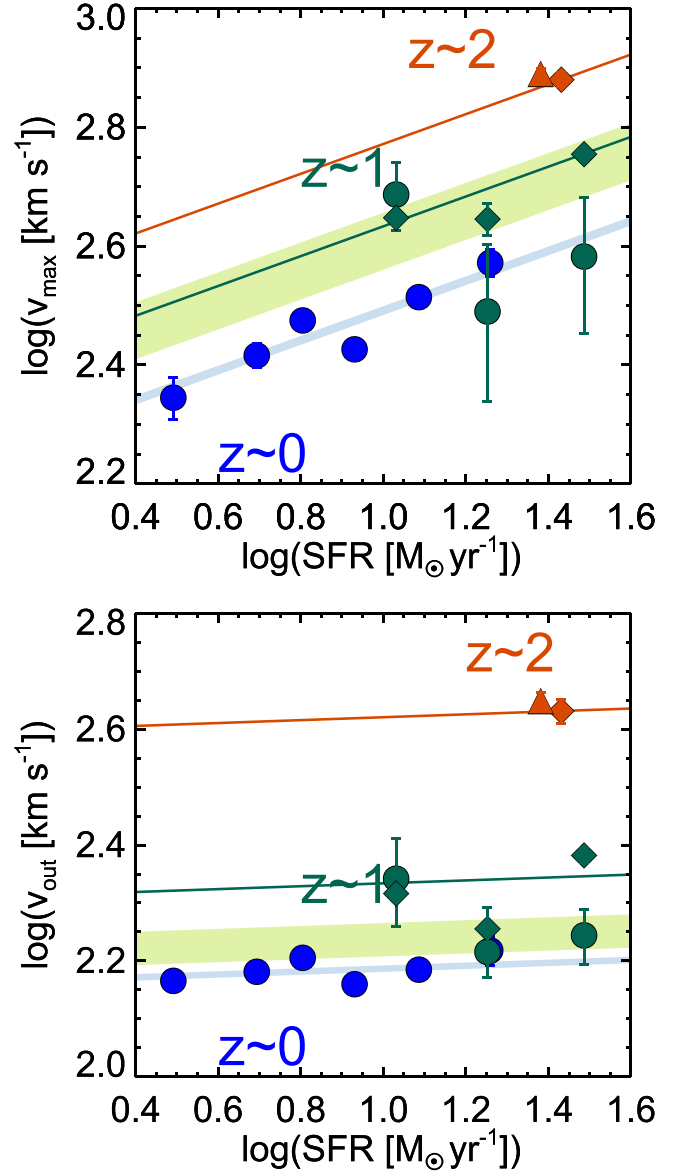
4.2. Evolution of Outflow Velocity

We show v_{max} measurements of our $z0$-, $z1$-, and $z2$-samples as a function of SFRs with the blue, green, and orange symbols, respectively, in the top panel of Figure 8. The bottom panel is the same as the top panel, but for v_{out}. Figure 8 indicates the increasing trend of the outflow velocity with increasing redshift. Martin & Bouché (2009) and Chisholm et al. (2016) indicate that the outflow velocity depends on the depths of the absorption lines, whereas Tanner et al. (2016) show that the outflow velocity depends on ionization energy (IE) of the ions used for velocity measurements. For these reasons, we compare the outflow velocities of the absorption lines that have similar depths and IE, which is presented in Figure 4. The details of our comparisons are explained below.

To compare the $z0$- with $z1$-samples, we use v_{max} and v_{out} computed from Na I D (IE $\simeq$ 5.1 eV) and Mg I (IE $\simeq$ 7.6 eV) absorption lines, respectively, which are depicted with the circles in Figure 8. In Section 4.1, we obtain the best-fit parameter sets of the scaling relation $V = V_1 \, SFR^{\alpha}$ for Na I D of the $z0$-sample: $V_1 = 174 \pm 9(145 \pm 12)$ and $\alpha = 0.25 \pm 0.04(0.03 \pm 0.03)$ for $V = v_{max} \, (v_{out})$. We perform a power-law fitting to $v_{max} \, (v_{out})$ for Na I D of the $z0$-sample and Mg I of the $z1$-sample with the slope fixed at $\alpha = 0.25(0.03)$. The best-fit parameter sets are $V_1 = 174 \pm 2(145 \pm 2)$ and $V_1 = 227 \pm 15(163 \pm 18)$ for Na I D and Mg I, respectively. The light-blue

Figure 7. Same as Figure 5, but for the central outflow velocities at $z \sim 2$. The orange diamond, triangle, and squares indicate the central outflow velocities of the $z2$-sample for C II, C IV, and Si II, respectively. Error bars denote the 1σ fitting errors. The open diamonds show the maximum outflow velocities of galaxies in Erb et al. (2012). The orange triangle is offset in SFR by 0.1 dex for clarity.

Figure 8. Same as Figure 5, but for the $z0$- (blue symbol), $z1$- (green symbol), and $z2$-samples (red symbol). Top: maximum outflow velocities as a function of SFRs. Each symbol corresponds to the elements of the absorption lines: Na I D (blue circle), Mg I (green circle), Mg II (green diamond), C II (orange diamond), and C IV (orange triangle). The circles, diamonds, and triangle indicate the velocities of elements that have low (5–7 eV), medium (15–24 eV), and high (48 eV) ionization energy, respectively. Error bars denote the 1σ fitting errors. The light-blue and light-green shades describe the result of the power-law fitting to Na I D and Mg I, respectively, with vertical 1σ fitting error range. The green and orange lines denote the best-fitting power-law function of Mg II and C II, respectively. Bottom: central outflow velocities as a function of SFRs. The symbols are the same as those in the top panel of this figure. In both panels, the orange triangles are offset in SFR by 0.05 dex for clarity.

and light-green shades in Figure 8 illustrate the best-fitting relations of Na I D at $z \sim 0$ and Mg I at $z \sim 1$, respectively. The widths of the shades represent the 1σ fitting error ranges. Figure 8 indicates that v_{max} (v_{out}) at $z \sim 1$ is significantly higher than the one at $z \sim 0$.

To compare the $z1$- and $z2$-samples, we use v_{max} and v_{out} computed from Mg II (IE $\simeq$ 15 eV) and C II (IE $\simeq$ 24 eV) absorption lines, respectively, which are depicted with the diamonds in Figure 8. In the same manner as Mg I of the $z1$-sample, we fit v_{max} (v_{out}) of Mg II by a power-law function with a slope fixed at $\alpha = 0.25(0.03)$. We obtain the best-fit parameters of $V_1 = 241 \pm 4(251 \pm 3)$ for $V = v_{max}$ (v_{out}). The green line in Figure 8 illustrates the best-fitting relations of Mg II at $z \sim 1$. For comparison, the orange line shows the line with $\alpha = 0.25(0.03)$ through the orange diamond. Figure 8

suggests that v_{max} (v_{out}) at $z \sim 2$ is significantly higher than the one at $z \sim 1$.

We note that Figure 8 illustrates a large difference of v_{out} between Mg II and C II. Since the systemic component in the C II line is larger than that in the Mg II line (Figure 4), this large systemic component may generate the high v_{out} value of C II. To evaluate outflow velocities with a small systemic component, we fit the C II line with $C_{f,sys} = 0.1$, which is the median of the best-fit $C_{f,sys}$ values at $z \sim 0$–1, and without the constraints on $b_{D,out}$. The best-fit $v_{max} (\simeq 719 \pm 39$ km s^{-1}) is

consistent with the values estimated without a constraint to $C_{f,\text{sys}}$. Thus, the v_{max} value is not affected by $C_{f,\text{sys}}$. Our conclusions do not change. On the other hand, v_{out} becomes small down to $\simeq 208 \pm 30$ km s^{-1}. We think that the results of v_{out} are easily affected by the systemic component and less reliable than those of v_{max}.

In summary, we find that v_{max} and v_{out} increase from $z \sim 0$ to 2. Although there is some implication of the redshift evolution of the outflow velocities (Rupke et al. 2005b; Du et al. 2016), this is the first time to identify the clear trend of the redshift evolution of the outflow velocities.

Here we discuss the effects of the selection biases. There are three sources of possible systematics that are included in our analysis. The first is the selection criterion of the SFR surface density Σ_{SFR} in the z0-sample. In Section 2.1, we select the galaxies with Σ_{SFR} larger than $10^{-0.8}\ M_\odot$ yr^{-1} kpc^{-2}, but we do not apply this criterion for the z1- and z2-samples. A large fraction of the z1-sample meets the criterion of Σ_{SFR} because the galaxies of the z1-sample have the median SFR of $\sim 7\ M_\odot$ yr^{-1} and the median Petrosian radius of 5.2 kpc estimated from photometry of some galaxies taken with *Hubble Space Telescope*/Advanced Camera for Surveys (Weiner et al. 2009). All of the members of our z2-sample also meet the criterion of Σ_{SFR} (Erb et al. 2006b). The second is the selection criterion of the inclination i in our z0-sample. We select the galaxies with $i < 30°$, which is less than the $60°$ that is the typical outflow opening angle of the SDSS galaxies (Chen et al. 2010). This criterion is likely not needed for the z1- and z2-samples because it is reported that the outflows of the galaxies at $z \sim 1$–2 are more spherical than those at $z \sim 0$ (Weiner et al. 2009; Martin et al. 2012; Rubin et al. 2014). In addition, the galaxies under these criteria of Σ_{SFR} and i should decrease the v_{max} and v_{out} of the z0-sample, indicating the redshift evolution of the outflow velocities more clearly. The third is the difference of instrumental resolutions. There is a possibility that low spectral resolutions may systematically increase the values of v_{max}. We convolve the highest-resolution ($R \sim 5000$) spectra of z1-sample with SDSS ($R \sim 2000$) and LRIS ($R \sim 800$) spectral resolutions and compare the v_{max} values of the original and the convolved spectra. In this way, we confirm that the systematics of the different spectral resolution is negligible in our results.

5. Discussion

5.1. Physical Origins of v_{max} Evolution

In Section 4.2, we find that the outflow velocities increase from $z \sim 0$ to 2. The power-law fitting to the results of Figure 8 gives

$$v_{\text{max}} \propto (1 + z)^{0.59 \pm 0.03} \qquad (8)$$

at a fixed SFR. This increasing trend of the outflow velocities is predicted by Barai et al. (2015), who carry out simulations with MUPPI and find that the outflow velocities increase from $z \sim 0.8$ to 3.0. We cannot quantitatively compare our results with those of the simulation because of the different definitions of the outflow velocity.

The redshift evolution of v_{max} is interpreted by an increase in Σ_{SFR} from $z \sim 0$ to 2. Shibuya et al. (2015) show that effective radii of galaxies decrease with increasing redshift by $r \propto (1 + z)^{-1}$ at a fixed stellar mass. On the assumption that a projected surface area of a disk galaxy is proportional to r^2,
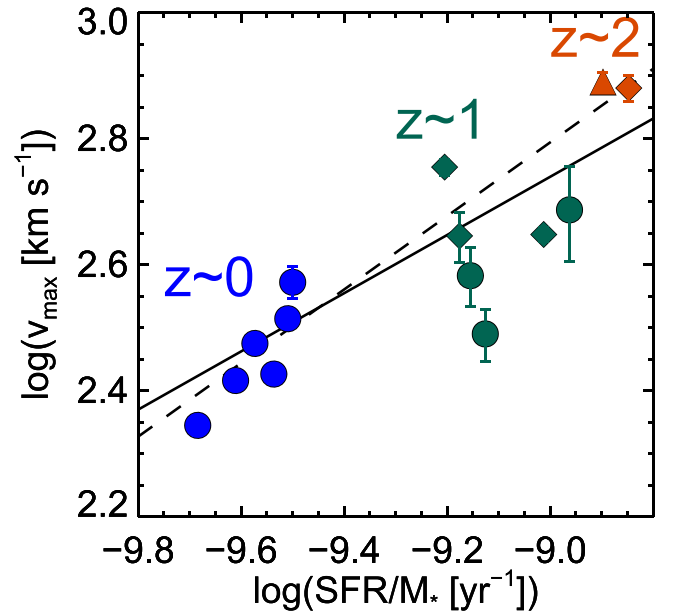
Figure 9. Outflow velocities as a function of SFR/M_*. The top and bottom panels show v_{max} and v_{out}, respectively. The symbols and colors are the same as those in Figure 8. In both panels, the green diamonds and the orange triangles are offset in SFR/M_* by 0.05 dex for clarity.

Σ_{SFR} increases with increasing redshift by $\Sigma_{\text{SFR}} \propto (1 + z)^2$ at a fixed stellar mass for a given SFR. Assuming the relation of $v_{\text{max}} \propto \Sigma_{\text{SFR}}^{1/3}$ at $z = 0$ found by Heckman & Borthakur (2016), we obtain a scaling relation expressing the evolution of the outflow velocity by

$$v_{\text{max}} \propto (1 + z)^{2/3}. \qquad (9)$$

Equation (9) is similar to Equation (8), albeit with a slight difference of the power. This simple calculation suggests that the v_{max} evolution originates from the Σ_{SFR} (i.e., size) evolution of galaxies.

This interpretation also predicts a relation between v_{max} and SFR/M_* at $z \sim 0$–2. At a fixed stellar mass of $\log(M_*/M_\odot) = 10.5$, Speagle et al. (2014) find

$$\text{SFR}/M_* \propto (1 + z)^{2.8}. \qquad (10)$$

Using Equations (9)–(10) and the relation of $v_{\text{max}} \propto \text{SFR}^{1/3}$ at $z = 0$ found by Heckman & Borthakur (2016), we obtain the v_{max} values increasing by

$$v_{\text{max}} \propto (1 + z)^{1.6} \qquad (11)$$

at a fixed stellar mass from $z \sim 0$ to 2. Comparing Equations (10) and (11) finally yields

$$v_{\text{max}} \propto \text{SFR}/M_*^{0.57} \qquad (12)$$

at a fixed stellar mass from $z \sim 0$ to 2. Figure 9 illustrates our fitting results of v_{max} as a function of SFR/M_*. We fit all data points of the z0-, z1-, and z2-samples with the form of $\log v_{\text{max}} \propto \beta \log \text{SFR}/M_*$. The best-fitting scaling factor is $\beta = 0.46 \pm 0.02$ (solid line in Figure 9). This β value is similar to the one of Equation (12). Moreover, if we use data points of only the z0- and z2-samples, we obtain $\beta = 0.58 \pm 0.02$ (dashed line in Figure 9), which is in excellent agreement with the one of Equation (12). These

results also support the interpretation that an increase in v_{max} is caused by an increase in Σ_{SFR} of galaxies from $z \sim 0$ to 2.

5.2. Mass Loading Factor

Another important parameter of the outflows is the mass loading factor η, which is defined by

$$\eta = \dot{M}_{out}/SFR, \quad (13)$$

where $\dot{M}_{out}$ is the mass outflow rate. η represents how the outflows contribute the feedback process of the galaxy formation and evolution. Estimates of η depend on assumptions of parameters. Our aim is, under the set of the fiducial parameters, to compare our observational results with theoretical predictions on the redshift evolution of the mass loading factors (Barai et al. 2015; Mitra et al. 2015; Muratov et al. 2015).

We estimate η by following previous studies that adopt the "down-the-barrel" technique (e.g., Weiner et al. 2009; Martin et al. 2012; Rubin et al. 2014). We use the absorption lines of Na I D, Mg I, and C II to calculate η of the z0-, z1-, and z2-samples, respectively. Although IE (depth) of C II is higher (deeper) than that of Na I D and Mg I, we directly compare the values of η estimated from the lines. This is because Figure 8 shows that v_{out} of Mg I and Mg II are comparable despite their different IEs and depths of the absorption lines.

To estimate $\dot{M}_{out}$, we use the spherical flow model (Rupke et al. 2002; Martin et al. 2012) that assumes the bi-conical outflow whose solid angle subtended by the outflowing gas is given by Ω. In the model, $\dot{M}_{out}$ is given by

$$\dot{M}_{out} = \bar{m}_p \Omega C_f v_{out} R N(H), \quad (14)$$

where $\bar{m}_p$ is the mean atomic weight, R is the inner radius of the outflows, and $N(H)$ is the column density of hydrogen. We assume $\bar{m}_p = 1.4$ amu and $\Omega = 4\pi$, which is a case of a spherical outflow. We also assume that R is the same as the effective radius that is obtained from the r_e–M_* relation of Shibuya et al. (2015).

We estimate $N(H)$ from the column density of an ion X^n, which is expressed as

$$N(X^n) = \frac{\tau_0 b_D}{1.497 \times 10^{-15} \lambda_{sys} f}, \quad (15)$$

where f is the oscillator strength. The oscillator strengths are taken from Morton (1991). We define the gas-phase abundance of an element X with respect to hydrogen as $(X/H)_{gas} \equiv N(X)/N(H)$, where the column density of an element $N(X)$ is given by $N(X) = \sum_n N(X^n)$. $N(X^n)$ can be converted into $N(H)$ with three parameters: the ionization fraction $\chi(X^n) \equiv N(X^n)/N(X)$, the dust depletion factor $d(X) \equiv (X/H)_{gas}/(X/H)_c$, and the cosmic metallicity at each redshift $\mu(X) \equiv (X/H)_c$, where the index c refers to the cosmic average. We thus estimate $N(H)$ with

$$N(H) = \frac{N(X^n)}{\chi(X^n) d(X) \mu(X)}. \quad (16)$$

Because it is difficult to obtain these three parameters by observations, we adopt fiducial parameters for our calculations as our best estimate. We use the solar metallicity for $\mu(X)$ of the z0-sample and half of the solar metallicity for $\mu(X)$ of the
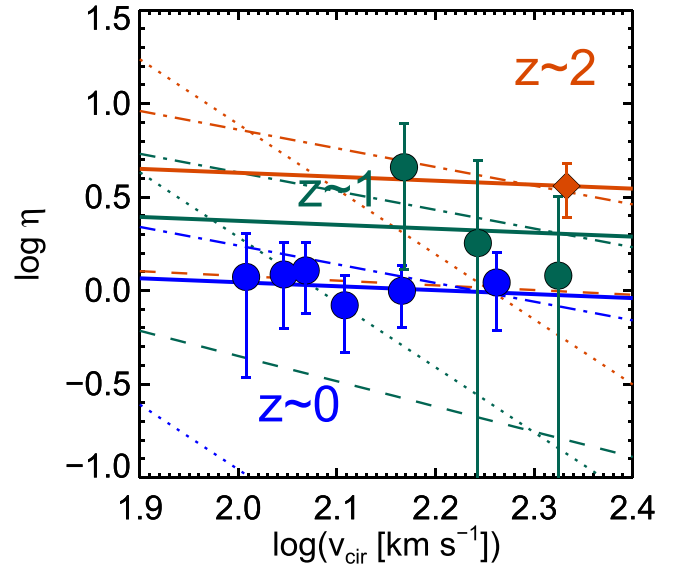
Figure 10. Mass loading factor as a function of v_{cir}. The data points are the same as those in Figure 8. The colors of blue, green, and orange correspond to $z \sim 0$, 1, and 2, respectively. The solid lines denote the linear-square fitting results. The dot-dashed, dashed, and dotted lines indicate the models presented by Muratov et al. (2015), Barai et al. (2015), and Mitra et al. (2015), respectively.

z1- and z2-samples, i.e., $\mu(X) = 0.5(X/H)_\odot$. According to Morton (2003), the solar metallicity values are $\log(Na/H)_\odot = -5.68$, $\log(Mg/H)_\odot = -4.42$, and $\log(C/H)_\odot = -3.48$. The dust depletion factors are scaled to Milky Way values taken from Savage & Sembach (1996): $d(Na) = 0.1$, $d(Mg) = 0.03$, and $d(C) = 0.4$. For the ionization fractions, we take the moderate value of $\chi(Na I D) = 0.1$, because photoionization models calculated by CLOUDY (Ferland et al. 1998, 2013) suggest $\chi(Na I D) = 10^{-4}$–1 (Murray et al. 2007; Chisholm et al. 2016). Given a high ionization parameter at $z \gtrsim 1$ (Nakajima & Ouchi 2014), we choose $\chi(Mg I) = 0.05$, a half of $\chi(Na I D)$. Chisholm et al. (2016) also find $\chi(Si II) \simeq 0.2$. Because the IEs of Si II (16 eV) and C II (24 eV) are comparable, we assume $\chi(C II) = 0.2$, which is the same as Si II. In summary, the parameters for Na I D, Mg I, and C II are $(\chi, d, \mu) = (0.1, 0.1, 2.1 \times 10^{-6})$, $(0.1, 0.03, 1.9 \times 10^{-5})$, and $(0.2, 0.4, 1.7 \times 10^{-4})$, respectively. $N(H)$ is calculated by Equation (16) with the parameter sets (χ, d, μ).

We estimate $\dot{M}_{out}$ by Equation (14) with C_f and v_{out}, which are derived in Section 3.2, and obtain η by Equation (13). We find that our samples have $0 \lesssim \log \eta \lesssim 1$, which is consistent with the results of previous studies (e.g., Heckman et al. 2015). Figure 10 shows η as a function of the halo circular velocity v_{cir}. The values of v_{cir} are calculated from M_*, with the M_*–M_h relation in Behroozi et al. (2013) and Equation (1) in Mo & White (2002). We perform the power-law fitting between η and v_{cir} of the z0-sample and obtain the best-fitting relation $\eta = \eta_1 v_{cir}^a$ for $\eta_1 = 2.9 \pm 16.3$ and $a = -0.2 \pm 1.1$. This scaling relation is consistent with the previous studies within the 1σ uncertainties: $a = -0.98$ for strong outflows investigated with the UV observations of the local galaxies (Heckman et al. 2015) and $a = -1.0$ for $v_{cir} > 60$ km s^{-1} found with the FIRE simulations (Muratov et al. 2015). Our result, $a = -0.2 \pm 1.1$, is weak evidence of a decreasing trend, although it is consistent with no correlation, i.e., $a = 0$. Our result is consistent with the momentum-driven model ($a = -1$). It is not conclusive, but we can rule out the

energy-driven model ($a = -2$) at the 90th percentile significance level. We also plot the data of the $z1$- and $z2$-samples in Figure 10, but we cannot discuss the scaling relation of them as a result of having few data points.

5.3. Physical Origins of η Evolution

Our observational results in Figure 10 indicate that η increases from $z \sim 0$ to 2 at a given circular velocity. We fit the $z0$-, $z1$-, and $z2$-samples with a power-law function $\eta = \eta_1 v_{\rm cir}^a$ at the fixed slope of $a = -0.2$, which is the best-fit parameter of the $z0$-sample (Section 5.2). We obtain the best-fit parameters $\eta_1 = 2.9 \pm 0.5$, 6.3 ± 4.5, and 11.3 ± 3.6 for the $z0$-, $z1$-, and $z2$-samples, which are illustrated in Figure 10 with the blue, green, and orange solid lines, respectively. The redshift evolution of η is obtained as $\eta \propto (1 + z)^{1.2 \pm 0.3}$ by a power-law fitting.

Theoretical methods predict an increase in the mass loading factors with increasing redshift (Barai et al. 2015; Mitra et al. 2015; Muratov et al. 2015). Our results reproduce the redshift evolution trend predicted by the theoretical studies. In particular, the relation $\eta \propto (1 + z)^{1.3}$ found by Muratov et al. (2015) is in good agreement with our results (Figure 10). Since our estimates, however, include large uncertainties, we cannot constrain the theoretical models from the observations.

Some theoretical models suggest that a large amount of gas increases $v_{\rm out}$, $v_{\rm max}$, and η toward high redshift. Barai et al. (2015) claim that gas-rich galaxies at high redshift launch outflows with high $v_{\rm out}$ and η. Similarly, Hayward & Hopkins (2017) find that the value of η increases exponentially by the increase in the gas fractions toward high redshift.

We discuss the redshift evolution of the outflows, SFR, and mass of cool gas in a galaxy. If we assume that $\dot{M}_{\rm out}$ is proportional to cool H I gas mass $M_{\rm gas}^{\rm cool}$, we can rewrite Equation (13) as

$$\eta = \frac{\dot{M}_{\rm out}}{\rm SFR} \propto \frac{M_{\rm gas}^{\rm cool} v_{\rm out}}{\rm SFR}. \qquad (17)$$

Hence, the mass of the cool gas in the galaxy is

$$M_{\rm gas}^{\rm cool} \propto \frac{\eta {\rm SFR}}{v_{\rm out}}. \qquad (18)$$

Below we calculate the redshift dependence of SFR, $v_{\rm out}$, η, and $M_{\rm gas}^{\rm cool}$ at a fixed stellar mass $\log(M_*/M_\odot) = 10.5$. The redshift evolution of SFR is given by Equation (10). If we assume that $v_{\rm out}$ and $v_{\rm max}$ follow the same dependence on z, the evolution of outflow velocities is expressed as Equation (11). We obtain $\eta \propto (1 + z)^{1.2 \pm 0.3} v_{\rm cir}^{-0.2 \pm 1.1}$, fitting the power-law functions to the results of Figure 10. Based on the estimates of the relation of $v_{\rm cir} \propto (1 + z)^{0.53 \pm 0.09}$ that we estimate from the M_*–M_h relation in Behroozi et al. (2013), η is written as $\eta \propto (1 + z)^{1.1 \pm 0.7}$. Substituting this equation and Equations (10) and (11) into Equation (18), we obtain the redshift dependence of $M_{\rm gas}^{\rm cool}$ by

$$M_{\rm gas}^{\rm cool} \propto (1 + z)^{2.3 \pm 0.7}. \qquad (19)$$

Equation (19) suggests that increasing $M_{\rm gas}^{\rm cool}$ causes the increases in outflow velocities, mass loading factors, and SFR with increasing redshift. This increasing trend of $M_{\rm gas}^{\rm cool}$ is consistent with independent observational results. If we assume that the molecular gas mass is proportional to $M_{\rm gas}^{\rm cool}$ at a given

stellar mass, there is a relation of $M_{\rm gas}^{\rm cool} \propto (1 + z)^{2.7}$ obtained by the radio observations of Genzel et al. (2015). This relation is consistent with Equation (19) within the 1σ uncertainty.

As noted in Section 5.2, however, the parameter sets used for deriving η include large uncertainties. The total uncertainty of $\chi(X^n)$, $d(X)$, and $\mu(X)$ is $\gtrsim 0.5$ dex. We thus think that the conclusion of an increase in η is not strong. However, we can securely claim that the theoretical models are consistent with our observational results under the assumption of the fiducial parameter sets shown in Section 5.2.

6. Summary

We investigate redshift evolution of galactic outflows at $z \sim 0$–2 in the same stellar mass range. We use rest-frame UV and optical spectra of star-forming galaxies at $z \sim 0$, 1, and 2 taken from the SDSS DR7, the DEEP2 DR4, and Erb et al. (2006a, 2006b), respectively. The outflows are identified with metal absorption lines: Na I D for the $z \sim 0$ galaxies, Mg I and Mg II for the $z \sim 2$ galaxies, and C II and C IV for the $z \sim 2$ galaxies. We construct composite spectra and measure the parameters of the galactic outflow properties such as the outflow velocities by the multicomponent fitting with the aid of the SSP models. Our results are summarized below.

1. We find that there are scaling relations between the outflow velocities and SFR at $z \sim 0$: for the maximum outflow velocity $v_{\rm max}$ by $v_{\rm max} \propto {\rm SFR}^{0.25 \pm 0.04}$ and for the central outflow velocity $v_{\rm out}$ by $v_{\rm out} \propto {\rm SFR}^{0.03 \pm 0.03}$. The velocities $v_{\rm max}$ and $v_{\rm out}$ are consistent with previous studies.

2. We confirm that both of the outflow velocities increase with increasing redshift. Because ions with higher IE likely trace higher-velocity clouds, we compare ions with similar ionization energies: Na I D (IE $\simeq$ 5.1 eV) and Mg I (IE $\simeq$ 7.6 eV) from $z \sim 0$ to 1, and Mg II (IE $\simeq$ 15 eV) and C II (IE $\simeq$ 24 eV) from $z \sim 1$ to 2. The velocities $v_{\rm max}$ and $v_{\rm out}$ at $z \sim 1$ ($z \sim 2$) are significantly higher than those at $z \sim 0$ ($z \sim 1$).

3. The increase in the outflow velocities from $z \sim 0$ to 2 can be explained by the increase in $\Sigma_{\rm SFR}$ (i.e., a decrease of the galaxy size) toward high redshift.

4. To calculate the mass loading factors η, we use Na I D at $z \sim 0$, Mg I at $z \sim 1$, and C II at $z \sim 2$. We then find that the scaling relation between η and the halo circular velocity $v_{\rm cir}$ is given by $\eta \propto v_{\rm cir}^a$ for $a = -0.2 \pm 1.1$ at $z \sim 0$. The slope of $a = -0.2 \pm 1.1$ suggests that the outflows of the SDSS galaxies are launched by a mechanism based on the momentum-driven model, which predicts $a = -1$.

5. We identify the increase in η from $z \sim 0$ to 2. The values of η increase by $\eta \propto (1 + z)^{1.2 \pm 0.3}$, with the fiducial parameter sets assumed in Section 5.2. Note that the parameter sets include large uncertainties.

6. We find the increases in $v_{\rm out}$, $v_{\rm max}$, and η toward high redshift by observations. These results are consistent with theoretical predictions that explain the evolution by the increase in gas in high-redshift galaxies.

ORCID iDs

Yuma Sugahara ⓘ https://orcid.org/0000-0001-6958-7856
Masami Ouchi ⓘ https://orcid.org/0000-0002-1049-6658
Lihwai Lin ⓘ https://orcid.org/0000-0001-7218-7407
Crystal L. Martin ⓘ https://orcid.org/0000-0001-9189-7818
Yuichi Harikane ⓘ https://orcid.org/0000-0002-6047-430X
Renbin Yan ⓘ https://orcid.org/0000-0003-1025-1711

References

Abazajian, K., Adelman-McCarthy, J. K., Agüeros, M. A., et al. 2004, AJ, 128, 502

Abazajian, K. N., Adelman-McCarthy, J. K., Agüeros, M. A., et al. 2009, ApJS, 182, 543
Adelberger, K. L., Steidel, C. C., Shapley, A. E., et al. 2004, ApJ, 607, 226
Alexandroff, R. M., Heckman, T. M., Borthakur, S., Overzier, R., & Leitherer, C. 2015, ApJ, 810, 104
Barai, P., Monaco, P., Murante, G., Ragagnin, A., & Viel, M. 2015, MNRAS, 447, 266
Behroozi, P. S., Wechsler, R. H., & Conroy, C. 2013, ApJ, 770, 57
Blanton, M. R., & Roweis, S. 2007, AJ, 133, 734
Bordoloi, R., Lilly, S. J., Hardmeier, E., et al. 2014, ApJ, 794, 130
Bouché, N., Hohensee, W., Vargas, R., et al. 2012, MNRAS, 426, 801
Breitschwerdt, D., McKenzie, J. F., & Voelk, H. J. 1991, A&A, 245, 79
Brinchmann, J., Charlot, S., White, S. D. M., et al. 2004, MNRAS, 351, 1151
Bruzual, G., & Charlot, S. 2003, MNRAS, 344, 1000
Calzetti, D., Armus, L., Bohlin, R. C., et al. 2000, ApJ, 533, 682
Chabrier, G. 2003, PASP, 115, 763
Chen, Y.-M., Tremonti, C. A., Heckman, T. M., et al. 2010, AJ, 140, 445
Chevalier, R. A., & Clegg, A. W. 1985, Natur, 317, 44
Chisholm, J., Tremonti, C. A., Leitherer, C., Chen, Y., & Wofford, A. 2016, MNRAS, 457, 3133
Chisholm, J., Tremonti, C. A., Leitherer, C., et al. 2015, ApJ, 811, 149
Ciddor, P. E. 1996, ApOpt, 35, 1566
Coil, A. L., Newman, J. A., Kaiser, N., et al. 2004, ApJ, 617, 765
Coil, A. L., Weiner, B. J., Holz, D. E., et al. 2011, ApJ, 743, 46
Cooper, M. C., Newman, J. A., Davis, M., Finkbeiner, D. P., & Gerke, B. F. 2012, spec2d: DEEP2 DEIMOS Spectral Pipeline, Astrophysics Source Code Library, ascl:1203.003
Davis, M., Faber, S. M., Newman, J., et al. 2003, Proc. SPIE, 4834, 161
Davis, M., Guhathakurta, P., Konidaris, N. P., et al. 2007, ApJL, 660, L1
de Vaucouleurs, G. 1948, AnAp, 11, 247
Du, X., Shapley, A. E., Martin, C. L., & Coil, A. L. 2016, ApJ, 829, 64
Erb, D. K., Quider, A. M., Henry, A. L., & Martin, C. L. 2012, ApJ, 759, 26
Erb, D. K., Steidel, C. C., Shapley, A. E., et al. 2006a ApJ, 646, 107
Erb, D. K., Steidel, C. C., Shapley, A. E., et al. 2006b ApJ, 647, 128
Faber, S. M., Phillips, A. C., Kibrick, R. I., et al. 2003, Proc. SPIE, 4841, 1657
Ferland, G. J., Korista, K. T., Verner, D. A., et al. 1998, PASP, 110, 761
Ferland, G. J., Porter, R. L., van Hoof, P. A. M., et al. 2013, RMxAA, 49, 137
Fukugita, M., Ichikawa, T., Gunn, J. E., et al. 1996, AJ, 111, 1748
Genzel, R., Tacconi, L. J., Lutz, D., et al. 2015, ApJ, 800, 20
Grimes, J. P., Heckman, T., Aloisi, A., et al. 2009, ApJS, 181, 272
Gunn, J. E., Carr, M., Rockosi, C., et al. 1998, AJ, 116, 3040
Hayward, C. C., & Hopkins, P. F. 2017, MNRAS, 465, 1682
Heckman, T. M. 2002, in ASP Conf. Ser. 254, Extragalactic Gas at Low Redshift, ed. J. S. Mulchaey & J. T. Stocke (San Francisco, CA: ASP), 292
Heckman, T. M., Alexandroff, R. M., Borthakur, S., Overzier, R., & Leitherer, C. 2015, ApJ, 809, 147
Heckman, T. M., Armus, L., & Miley, G. K. 1990, ApJS, 74, 833
Heckman, T. M., & Borthakur, S. 2016, ApJ, 822, 9
Heckman, T. M., Lehnert, M. D., Strickland, D. K., & Armus, L. 2000, ApJS, 129, 493
Ipavich, F. M. 1975, ApJ, 196, 107
Jones, T. A., Ellis, R. S., Schenker, M. A., & Stark, D. P. 2013, ApJ, 779, 52
Kacprzak, G. G., Martin, C. L., Bouché, N., et al. 2014, ApJL, 792, L12
Kauffmann, G., Heckman, T. M., White, S. D. M., et al. 2003, MNRAS, 341, 33
Kornei, K. A., Shapley, A. E., Martin, C. L., et al. 2012, ApJ, 758, 135
Kroupa, P. 2001, MNRAS, 322, 231
Larson, R. B. 1974, MNRAS, 169, 229
Law, D. R., Steidel, C. C., Shapley, A. E., et al. 2012, ApJ, 759, 29
Lehnert, M. D., & Heckman, T. M. 1996a, ApJ, 462, 651
Lehnert, M. D., & Heckman, T. M. 1996b, ApJ, 472, 546
Leitherer, C., Ortiz Otálvaro, P. A., Bresolin, F., et al. 2010, ApJS, 189, 309
Lin, L., Koo, D. C., Weiner, B. J., et al. 2007, ApJL, 660, L51
Maraston, C., Nieves Colmenárez, L., Bender, R., & Thomas, D. 2009, A&A, 493, 425
Maraston, C., & Strömbäck, G. 2011, MNRAS, 418, 2785
Markwardt, C. B. 2009, in ASP Conf. Ser. 411, Astronomical Data Analysis Software and Systems XVIII, ed. D. A. Bohlender, D. Durand, & P. Dowler (San Francisco, CA: ASP), 251
Martin, C. L. 1998, ApJ, 506, 222
Martin, C. L. 2005, ApJ, 621, 227
Martin, C. L. 2006, ApJ, 647, 222
Martin, C. L., & Bouché, N. 2009, ApJ, 703, 1394
Martin, C. L., Shapley, A. E., Coil, A. L., et al. 2012, ApJ, 760, 127
McLean, I. S., Becklin, E. E., Bendiksen, O., et al. 1998, Proc. SPIE, 3354, 566

Mitra, S., Davé, R., & Finlator, K. 2015, MNRAS, 452, 1184
Mo, H. J., & White, S. D. M. 2002, MNRAS, 336, 112
Morton, D. C. 1991, ApJS, 77, 119
Morton, D. C. 2003, ApJS, 149, 205
Mostek, N., Coil, A. L., Moustakas, J., Salim, S., & Weiner, B. J. 2012, ApJ, 746, 124
Muratov, A. L., Kereš, D., Faucher-Giguère, C.-A., et al. 2015, MNRAS, 454, 2691
Murray, N., Martin, C. L., Quataert, E., & Thompson, T. A. 2007, ApJ, 660, 211
Murray, N., Quataert, E., & Thompson, T. A. 2005, ApJ, 618, 569
Muzahid, S., Kacprzak, G. G., Churchill, C. W., et al. 2015, ApJ, 811, 132
Nakajima, K., & Ouchi, M. 2014, MNRAS, 442, 900
Newman, J. A., Cooper, M. C., Davis, M., et al. 2013, ApJS, 208, 5
Oppenheimer, B. D., & Davé, R. 2006, MNRAS, 373, 1265
Padilla, N. D., & Strauss, M. A. 2008, MNRAS, 388, 1321
Rubin, K. H. R., Prochaska, J. X., Koo, D. C., et al. 2014, ApJ, 794, 156
Rubin, K. H. R., Weiner, B. J., Koo, D. C., et al. 2010, ApJ, 719, 1503
Rupke, D. S., Veilleux, S., & Sanders, D. B. 2002, ApJ, 570, 588
Rupke, D. S., Veilleux, S., & Sanders, D. B. 2005a, ApJS, 160, 87
Rupke, D. S., Veilleux, S., & Sanders, D. B. 2005b, ApJS, 160, 115
Salim, S., Rich, R. M., Charlot, S., et al. 2007, ApJS, 173, 267
Salpeter, E. E. 1955, ApJ, 121, 161
Sato, T., Martin, C. L., Noeske, K. G., Koo, D. C., & Lotz, J. M. 2009, ApJ, 696, 214
Savage, B. D., & Sembach, K. R. 1996, ARA&A, 34, 279
Schaye, J., Crain, R. A., Bower, R. G., et al. 2015, MNRAS, 446, 521
Schroetter, I., Bouché, N., Péroux, C., et al. 2015, ApJ, 804, 83
Schroetter, I., Bouché, N., Wendt, M., et al. 2016, ApJ, 833, 39
Schwartz, C. M., & Martin, C. L. 2004, ApJ, 610, 201
Schwartz, C. M., Martin, C. L., Chandar, R., et al. 2006, ApJ, 646, 858
Shapley, A. E., Steidel, C. C., Pettini, M., & Adelberger, K. L. 2003, ApJ, 588, 65
Shibuya, T., Ouchi, M., & Harikane, Y. 2015, ApJS, 219, 15
Shibuya, T., Ouchi, M., Nakajima, K., et al. 2014, ApJ, 788, 74
Somerville, R. S., & Davé, R. 2015, ARA&A, 53, 51
Speagle, J. S., Steinhardt, C. L., Capak, P. L., & Silverman, J. D. 2014, ApJS, 214, 15
Springel, V., & Hernquist, L. 2003, MNRAS, 339, 289
Springel, V., White, S. D. M., Jenkins, A., et al. 2005, Natur, 435, 629
Steidel, C. C., Adelberger, K. L., Shapley, A. E., et al. 2003, ApJ, 592, 728
Steidel, C. C., Erb, D. K., Shapley, A. E., et al. 2010, ApJ, 717, 289
Steidel, C. C., Shapley, A. E., Pettini, M., et al. 2004, ApJ, 604, 534
Steidel, C. C., Strom, A. L., Pettini, M., et al. 2016, ApJ, 826, 159
Strauss, M. A., Weinberg, D. H., Lupton, R. H., et al. 2002, AJ, 124, 1810
Tanner, R., Cecil, G., & Heitsch, F. 2016, ApJ, 821, 7
Tremonti, C. A., Heckman, T. M., Kauffmann, G., et al. 2004, ApJ, 613, 898
Tremonti, C. A., Moustakas, J., & Diamond-Stanic, A. M. 2007, ApJL, 663, L77
Wadepuhl, M., & Springel, V. 2011, MNRAS, 410, 1975
Weiner, B. J., Coil, A. L., Prochaska, J. X., et al. 2009, ApJ, 692, 187
Willmer, C. N. A., Faber, S. M., Koo, D. C., et al. 2006, ApJ, 647, 853
York, D. G., Adelman, J., Anderson, J. E., Jr., et al. 2000, AJ, 120, 1579